



Spatial precipitate separation enhanced by complex formation

Paszkał Papp^a, Ágota Tóth^a, Dezső Horváth^{b,*}

^aDepartment of Physical Chemistry and Materials Science, University of Szeged, Rerrich Béla tér 1., Szeged H-6720, Hungary

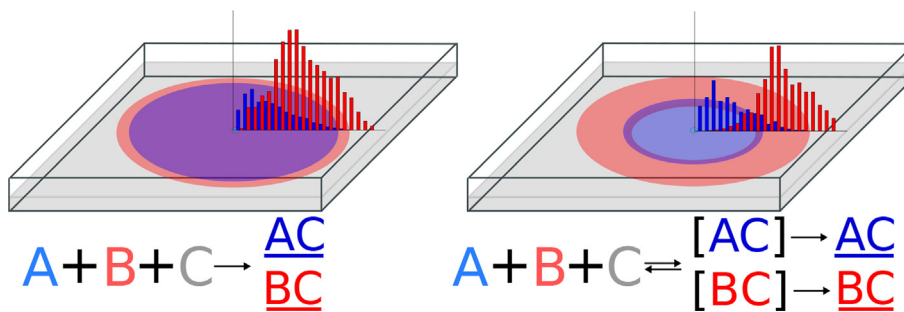
^bDepartment of Applied and Environmental Chemistry, University of Szeged, Rerrich Béla tér 1., Szeged H-6720, Hungary



HIGHLIGHTS

- Strategy based on complex formation is elaborated for separation in a flow reactor.
- CFD model is developed to describe spatial precipitate separation.
- Mean position and precipitate excess are introduced to measure extent of separation.
- Precipitate production and spatial separation can be controlled by injection rate.

GRAPHICAL ABSTRACT



ARTICLE INFO

Article history:

Received 18 January 2022

Received in revised form 19 July 2022

Accepted 23 July 2022

Available online 28 July 2022

Keywords:

Inorganic oxalate precursors
Computational fluid dynamics
Gravity current
Flow chemistry

ABSTRACT

The separation of inorganic precipitates with similar solubility products is a challenging task in chemical engineering. We present a computational fluid dynamics study of a precipitation reaction in a flow-driven reactor. For a reference study, the cobalt(II)-copper(II)-oxalate system is selected, where precipitation occurs simultaneously and the difference in solubility is within an order of magnitude as shown experimentally. For general description of two metal ions competing for one common anion, several parameters have been varied to identify the factors responsible for spatial separation. Two new quantities, the mean position of sedimented particles and the precipitation excess, are introduced to characterize the extent of separation. The calculations have shown that complex formation prior to nucleation makes the separation feasible for a wide range of thermodynamic or kinetic parameters. The injection rate can be used for fine tuning both the amounts of precipitate and their spatial separation when complexes are present.

© 2022 The Author(s). Published by Elsevier Ltd. This is an open access article under the CC BY-NC-ND license (<http://creativecommons.org/licenses/by-nc-nd/4.0/>).

1. Introduction

Precipitation reactions play a vital role in many industrial processes and in nature. For example nanosized ceramic powders (Acarbaş et al., 2007), biomaterials (López-Macipe et al., 1998), and catalysts (Dong et al., 2016; Jinwei et al., 2008) are routinely synthesized by chemical precipitation. Although precipitate formation in mammals is usually pathological, like kidney stone formation (Coe et al., 2005), crystal formation in plants includes

calcium regulation and protection against herbivory (Franceschi and Nakata, 2005). By coupling precipitation reaction with transport phenomena, like diffusion or advection, spatial gradients can develop. The nonequilibrium conditions maintained by the gradients give rise to various precipitate pattern formations (Baker et al., 2009; Nakouzi and Steinbock, 2016; Nabika et al., 2020), where symmetry breaking may occur resulting in spatially inhomogeneous precipitate distribution (Pótári et al., 2019; Brau et al., 2017).

In nature or in industry typically mixture of precipitates form where not only the chemical composition (Rakotozandry et al., 2020) but also crystal size and shape varies (Bohner et al., 2015).

* Corresponding author.

E-mail address: horvathd@chem.u-szeged.hu (D. Horváth).

The separation of precipitates with different chemical composition still poses a serious problem like in sewage sludge cleaning (Olgun and Atar, 2011). Industrially fractional crystallization (Cisternas et al., 2006) is used most commonly to temporally separate the precipitates, although for precipitates with similar solubilities additional chemicals are required to improve the separation, thus increasing the chance of contamination. Centrifugal precipitation chromatography (Ito and Qi, 2010) is a recently developed technique for spatial precipitate separation. However, the method is based on the components solubility in ammonium sulfate, and hence, mainly the separation of proteins can be achieved. The separation of cobalt and copper, for example, is challenging, in many cases requiring either expensive chemicals (Zhang et al., 2020), membranes (Duan et al., 2017), or ionic liquids (Diabate et al., 2020). Oxalic acid is a frequent precipitant of transition (Li et al., 2019; Bowen et al., 2010) or rare-earth (Yamada et al., 2018) metal ions as oxalates are typical precursors of metal oxides, which are widely used catalysts for different industrial processes (Prieto et al., 2014; Xiang et al., 2014; Chen et al., 2020). In nature transition metal oxalate precipitation plays an important role in biomineralisation. Some lichens have a unique ability to dissolve and then precipitate toxic elements as oxalate salts, thus granting a high tolerance against heavy-metals (Adamo and Violante, 2000; Sarret et al., 1998). Several wood-rotting fungi species have been used for bioremediation because they are capable of biotransforming toxic metal compounds into insoluble metal oxalates (Fomina et al., 2005; Kaewdoung et al., 2016; Gadd, 2007).

In this article we construct a model for studying precipitate separation in a flow-driven reactor even if the difference in the solubilities is less than an order of magnitude. The separation is achieved in a Hele-Shaw reactor, which is frequently used in chemical technology, environmental and biomedical engineering (Stergiou et al., 2022). For a base case the previously studied cobalt(II)-oxalate and copper(II)-oxalate system is selected, where precipitation takes place simultaneously (Tth-Szeles et al., 2017; Tth-Szeles, 2018). A homogeneous mixture of copper and cobaltous nitrate is injected into the initially stagnant pool of sodium oxalate solution from below leading to the radial separation of copper(II) oxalate (CuOx) and cobalt(II) oxalate (CoOx) precipitates under appropriate experimental conditions. This system requires building a CFD model that can handle both fast equilibrium processes in the fluid phase and slower precipitation reactions to yield reactive solid particles that can later grow in size, in addition to the regular fluid dynamics balance laws. The chosen oxalates not only are appropriate for the study due to their close solubility products ($K_{sp,CuOx} = 1.74 \times 10^{-3} \text{ mol}^2/\text{m}^6$ and $K_{sp,CoOx} = 2.61 \times 10^{-3} \text{ mol}^2/\text{m}^6$) but also exhibit great significance in several industrial fields.

A thorough study is then carried out with the model to identify the key parameters responsible for the separation in general. We systematically vary the flow rate, the particle shapes, and both the thermodynamic and the kinetic parameters to gain a deeper understanding of the spatial precipitate separation in flow-driven conditions.

2. Modeling study

A miscible fluid containing the homogeneous mixture of two reactants is pumped from below into a reactor which accommodates a third one as illustrated in Fig. 1. Upon contacting the injected reactants (M: A, B) with the one inside the reactor (C) leads to precipitation along with the simultaneous formation of solid particles with two different chemical composition, resulting a solid-liquid two-phase system. The laminar flow is governed by the Navier-Stokes equation for incompressible fluids ($\nabla \cdot \vec{u} = 0$) as

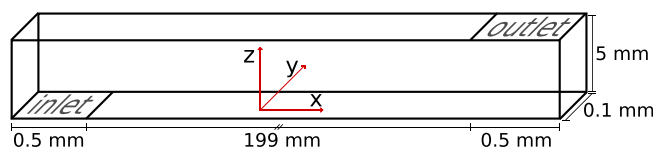


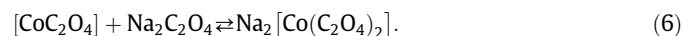
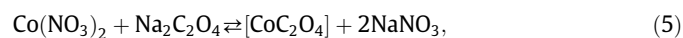
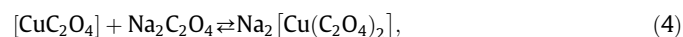
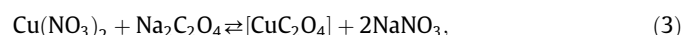
Fig. 1. The schematic presentation of the reactor.

$$\rho \frac{\partial \vec{u}}{\partial t} + \rho(\vec{u} \cdot \nabla)\vec{u} = \rho\nu\nabla^2\vec{u} - \nabla p + \rho\vec{g} + \vec{F} \quad (1)$$

where \vec{u} is the velocity of the fluid flow, p is the pressure, $\nu = 10^{-6} \text{ m}^2/\text{s}$ is the kinematic viscosity of the liquid, ρ is the density of the solutions, while $\vec{F} = \sum \vec{F}_i$ is the force per unit volume originating from the presence of solid particles. The drag force exerted on the liquid medium by an individual particle with density ρ_i is $\vec{F}_i = 3\rho C_D|\vec{u}_{p,i} - \vec{u}|/(4\rho_i d_i)$, where $\vec{u}_{p,i}$ is the velocity of the particle, d_i is the diameter of the sphere with the same volume as the particle and C_D is the drag coefficient. Haider and Levenspiel (1989) Dilute solutions have been used in the experiments, therefore, we can apply the Boussinesq approximation, according to which the liquid density only appears in the term containing the gravitational acceleration in Eq. (1); in all other terms ρ is replaced with ρ_0 , the density of the solvent water. At these concentrations the solution density is a linear function of the composition according to

$$\rho = \rho_0 + \sum \rho_i c_i \quad (2)$$

where ρ_i is the density contribution of species i with concentration c_i . In case of the previously mentioned cobalt(II)-, copper(II)-oxalate validating system at first fast complex formation occurs. Based on the experimental observations only the 1:1 and 1:2 metal(II):oxalate complexes (denoted in square brackets) form in significant amount according to the following reactions (Tth-Szeles et al., 2017):



The complex formation occurs on a much shorter timescale than the precipitation or the mixing, therefore, pre-equilibrium approximation can be used to obtain the concentrations of species. Although the counter ions do not take part in further reactions, their presence must be accounted for due to their contribution to density. Once the solution becomes supersaturated, nucleation will start slowly, followed by growth leading to a heterogeneous system according to



where underlines denote solid products. Although the precipitation reaction is reversible, dissolution has not been observed in the time span of the experiment, therefore approximating it as an irreversible step does not cause any discrepancy due to the permanent supersaturation.

The temporal change in the concentrations of $\text{Cu}(\text{NO}_3)_2$, $\text{Co}(\text{NO}_3)_2$, $\text{Na}_2\text{C}_2\text{O}_4$, NaNO_3 , $[\text{CuC}_2\text{O}_4]$, $[\text{CoC}_2\text{O}_4]$, $\text{Na}_2[\text{Cu}(\text{C}_2\text{O}_4)_2]$, and $\text{Na}_2[\text{Co}(\text{C}_2\text{O}_4)_2]$ can be described by the component balance equations

$$\frac{\partial c_i}{\partial t} + (\vec{u} \cdot \nabla)c_i = D_i\nabla^2 c_i + f_i(\mathbf{c}), \quad (9)$$

where the second term on the left side of the equation is the contribution of advection, while on the right side the diffusion and kinetic source terms are presented, respectively, with D_i being the diffusion coefficient of the i^{th} component. The kinetic source term incorporates the reaction rates (r_j) via $f_i = \sum_j v_{ij} r_j$. The reaction rates of the solid precipitate formation (r_7 and r_8) consist of two parts: the nucleation and the growth, with the latter depending on the particle shape. The experiments have shown that the cobalt(II) and copper(II) oxalate particles also differ in their shape (Toth-Szeles et al., 2017). The precipitation process generating spherical CuOx particles is governed by the rate equation

$$r_7 = k_{n,\text{CuOx}} S_{\text{CuOx}} + k_g \sum_i d_i^2 S_{\text{CuOx}}, \quad (10)$$

where $k_{n,\text{CuOx}}$ and k_g are the rate coefficients for nucleation and growth, respectively, while d_i is the diameter of the i^{th} spherical precipitate particle in the appropriate volume. The quantity $S = [\text{CuC}_2\text{O}_4] - K_{sp,\text{CuOx}} \beta_{\text{CuOx}}$ is the measure of supersaturation, where $K_{sp,\text{CuOx}}$ is the solubility product and β_{CuOx} is the stability constant for reaction (3). Eq. (10) is based on our earlier experimental work on oxalate precipitations (Das et al., 2020). In addition, the growth rate is also proportional to the surface area of the solid particles (Mullin, 2001). The reaction rate for the rectangular cuboid CoOx formation can be obtained in a similar manner as

$$r_8 = k_{n,\text{CoOx}} S_{\text{CoOx}} + \kappa_g S_{\text{CoOx}}, \quad (11)$$

where $\kappa_g = 2k_a \sum_i a_i^2 + 4k_b \sum_i a_i b_i$ with k_a being the growth rate coefficient of the smaller aa -face of the rectangular cuboid, k_b that of the larger ab -face, and $S_{\text{CoOx}} = [\text{CoC}_2\text{O}_4] - K_{sp,\text{CoOx}} \beta_{\text{CoOx}}$ with β_{CoOx} being the stability constant for reaction (5).

Both reactions in Eqs. (7) and (8) transform the single-phase system into a two-phase one. This gradual transition from a true solution to a heterogeneous system has to be split into two parts when we use governing equations based on mean field approximation. It is important to point out that we have to handle the transition of a continuous concentration field into discrete particle numbers while maintaining the component balance. Since interactions are not evaluated on the molecular level, particles can only be treated as a new phase when they grow to a size where van der Waals forces do not dominate, i.e., to the upper limit of colloid range. Below that, colloids are treated as solutes of a true solution and a concentration value is assigned to them as they move with the liquid phase as passive tracers.

In a given cell of the grid during an iteration step, the transition, i.e., the appearance of a discrete precipitate particle, only takes place if a new spherical CuOx particle with $d_j > 1 \mu\text{m}$ and/or a CoOx particle with a_j and $b_j > 1 \mu\text{m}$ can form.

With CuOx particles already present in the cell volume, growth takes place leading to an increase in the amount of substance (Δn_j) for the j^{th} precipitate particle as

$$\Delta n_j = \frac{k_g A_j}{k_{n,\text{CuOx}} + k_g \sum_r A_r} r_7 \Delta t, \quad (12)$$

where A_j is the surface of the j^{th} particle and Δt is the length of the iteration step. In the denominator the summation is for all CuOx particles with surface area A_r in the cell volume. A formula analogous to Eq. (12) is applicable to CoOx particles. For spherical CuOx, the diameter increment during an iteration step can be calculated from the volume change ΔV_j of the j^{th} particle as

$$\Delta d_j = \left(d_j^3 + \frac{6\Delta V_j}{\pi} \right)^{1/3} - d_j = \left(d_j^3 + \frac{6M\Delta n_j}{\pi\rho_p} \right)^{1/3} - d_j, \quad (13)$$

where M is the molar mass and ρ_p is the density of the precipitate. For the cuboid CoOx particles, the increment of both sides (Δa_j and Δb_j) is determined in an iterative way by applying Newton's method for the formula analogous to Eq. (13) (see supplementary material).

Eqs. (1) and (9) are solved by a finite volume method using the OpenFOAM software package (Weller et al., 1998). An operator splitting technique is applied for the last term in Eq. (9), since equilibrium conditions are maintained for Eqs. (3)–(6), in which case equilibrium constants are needed only for the calculation of the updated concentration field instead of the individual rate constants. Because the targeted experimental spatial separation exhibits radial symmetry with negligible contribution from curvature, we can use a rectangular model for a radially cut segment of the reactor. Therefore without loss of generality, a rectangular slab of $X \times Y \times Z = 200 \times 0.1 \times 5 \text{ mm}^3$ physical dimensions with $450 \times 1 \times 25$ volume element discretisation is constructed for the calculations, where transport in the y -direction is neglected, i.e., the fluid flow is effectively two-dimensional. With this choice we have selected the finest grid that still allows the handling of small solid particles. The in-house code, based on the PISO algorithm (Issa, 1986), incorporates Lagrangian particle tracking for processing the formation of solid particles. Since mutual interaction between the particles and the fluid is considered (two-way coupling) and the CoOx particles are anisotropic, the *NonSphereDragForce* library of OpenFOAM is modified. Based on Ref. (Haider and Levenspiel, 1989), for each individual particle the sphericity (ψ) – defined as the surface area of the volume equivalent sphere to that of the particle – is calculated to obtain the drag force coefficient C_D . The integration time step is adjusted so that solid particle generation remains independent of the spatial resolution of the grid. To introduce stochasticity to the system, the position of new particles is randomized with a factor varying between 0 and half of the cell size, thus particles can appear anywhere within the given cell volume. The particle density remains low in our system, therefore direct particle–particle interactions are neglected.

In the experiments, velocity is constantly decreasing due to the radial spreading. By using a reactor with a rectangular geometry (cf. Fig. 1), we can set a smaller linear injection rate ($u_z = u_{in} = 10^{-4} \text{ m/s}$), which can maintain a horizontal flow corresponding to that observed experimentally in the area where precipitate formation is the most dominant. The same constant value is set for the outflow, while at the bottom and the right side of the reactor, the fluid velocity is zero. At the top of the reactor *slip* boundary condition is used corresponding to the open liquid surface of the experiments, i.e., only the tangential component of the velocity vector is kept. A symmetry plane is placed at the left wall in analogy to the experimental setup. The stoichiometrically limiting species is the oxalate ion as the initial reactant concentrations are $c_{M^{2+}} = 0.4 \text{ mol/L}$ and $c_{\text{Ox}^{2-}} = 0.05 \text{ mol/L}$ according to the experiments. At the inlet Dirichlet, while at the outlet Neumann zero gradient boundary conditions are used for the concentration fields. The complex formation constants associated with Eqs. (3)–(6) are $\log_{10} \beta_{\text{CuOx}} = 4.84$, $\log_{10} \beta_{\text{CoOx}} = 3.25$, $\log_{10} \beta_{\text{CuOx}_2} = 9.21$, $\log_{10} \beta_{\text{CoOx}_2} = 5.60$ (Kotry and Sucha, 1985), i.e., $K_3 = \beta_{\text{CuOx}}$, $K_4 = \beta_{\text{CuOx}_2} / \beta_{\text{CuOx}}$, $K_5 = \beta_{\text{CoOx}}$, $K_6 = \beta_{\text{CoOx}_2} / \beta_{\text{CoOx}}$. The densities are listed in the supplementary material. The reaction rate constants for nucleation $k_{n,\text{CuOx}} = 15 \times 10^{-8} \text{ m}^3 / (\text{s mol})$, $k_{n,\text{CoOx}} = 3 \times 10^{-5} \text{ m}^3 / (\text{s mol})$ and for growth $k_g = 4 \times 10^6 \text{ m} / (\text{s mol})$, $k_a = 10^6 \text{ m} / (\text{s mol})$, $k_b = 2 \times 10^5 \text{ m} / (\text{s mol})$ have been chosen to match the past experimental observations of the individual CuOx and CoOx precipitation.

3. Results

During the simulations the solution containing Co(II) and Cu(II) metal ions are injected into the reactor, which contains sodium oxalate solution. The flow remains in the laminar regime because the Reynolds number, defined as $Re = uD_H/\nu$, falls in the range of 0.1–0.8, where $D_H = 4A/P$ is the hydraulic diameter with cross-sectional area A and wetted perimeter P . The injected fluid is denser than the solution inside the reactor, thus it spreads on the bottom of the reactor (see Fig. 2 a). The gravity current pushes the fluid inside the reactor upwards, creating a vortex at the parabola tip (Fig. 2 b), where the most intensive mixing occurs. The entire domain is sufficiently large, so the outlet has no effect on the flow field around the gravity current. Based on geometric spreading, a characteristic height can be associated with the gravity current, defined as the injected volume divided by the area it covers according to

$$\bar{h} = \frac{qt}{L_y d_x} = \frac{u_{in} d_{in} t}{d_x}, \quad (14)$$

where q is the volume flow rate of the injected liquid, $d_{in} = 0.5$ mm for the inlet, d_x is the distance traveled by the fluid flowing in the x -direction, and L_y is the width of the reactor. This characteristic height is only 0.13 mm at 100 s and 0.17 mm at 500 s. One can also associate a mean height with the concentration field (\bar{h}_c) within the current, defined by the position of the inflection point along the vertical direction. It is significantly greater than that of geometric spreading at the corresponding times (0.9 mm and 1.6 mm, respectively). This indicates that diffusion is the dominant transport process perpendicular to the flow, causing the thickening of the gravity current. Superimposed on the flow field of the gravity current is the flow caused by the sedimentation of solid particles. This is visible in Fig. 2b near the inlet close to the bottom, where some of the velocity vectors, instead of following the main streamlines, point downwards.

The injected Co(II) and Cu(II) ions react rapidly with the oxalate ions yielding various complexes with their concentration distribution presented in Fig. 3. The complex formation constant of oxalato copper(II) is greater than that of oxalato cobalt(II), thus the former forms closer to the bottom of the reactor. For the same reason, Co(II) ions have to diffuse further upwards to produce cobaltous oxalate. The same behavior is observed for the bis(oxalato) complexes, therefore, bis(oxalato) cobaltate(II) ions are always located above the bis(oxalato) cuprate(II) ions.

By utilizing the previously described thermodynamic parameters and fine tuning the rate constants for nucleation and growth (see values in the last paragraph of Sec. 2), we have managed to produce spatial precipitate separation which matches the past experimental observations (Tóth-Szeles et al., 2017) well (see Fig. 4). Hereafter, the parameter set used to calculate this distribution will be referred as the reference case. We point out that these distributions are related to number averages and, hence, mass averages or mass distributions would be different because of varying particle size. The calculated distribution still differs as particles sediment closer to the inlet because a rectangular reactor is considered and no velocity drop exists unlike in the case of radial spreading.

Taking the copper(II)–cobalt(II)–oxalate system as a base case, we can investigate the effect of different parameters on the spatial precipitate separation in general systems with the same reaction type, reactor geometry, and flow rate. In order to do that, solubility products (K_{sp}), complex equilibrium constants (β), nucleation (k_n) and growth rate coefficients (k_g or k_a, k_b) have been varied with one order of magnitude compared to the reference case. To characterize the extent of the spatial separation, we have first introduced the mean position of the sedimented MC (M: A, B) particles as

$$X_{MC} = \frac{\sum_i^N x_i}{N}, \quad (15)$$

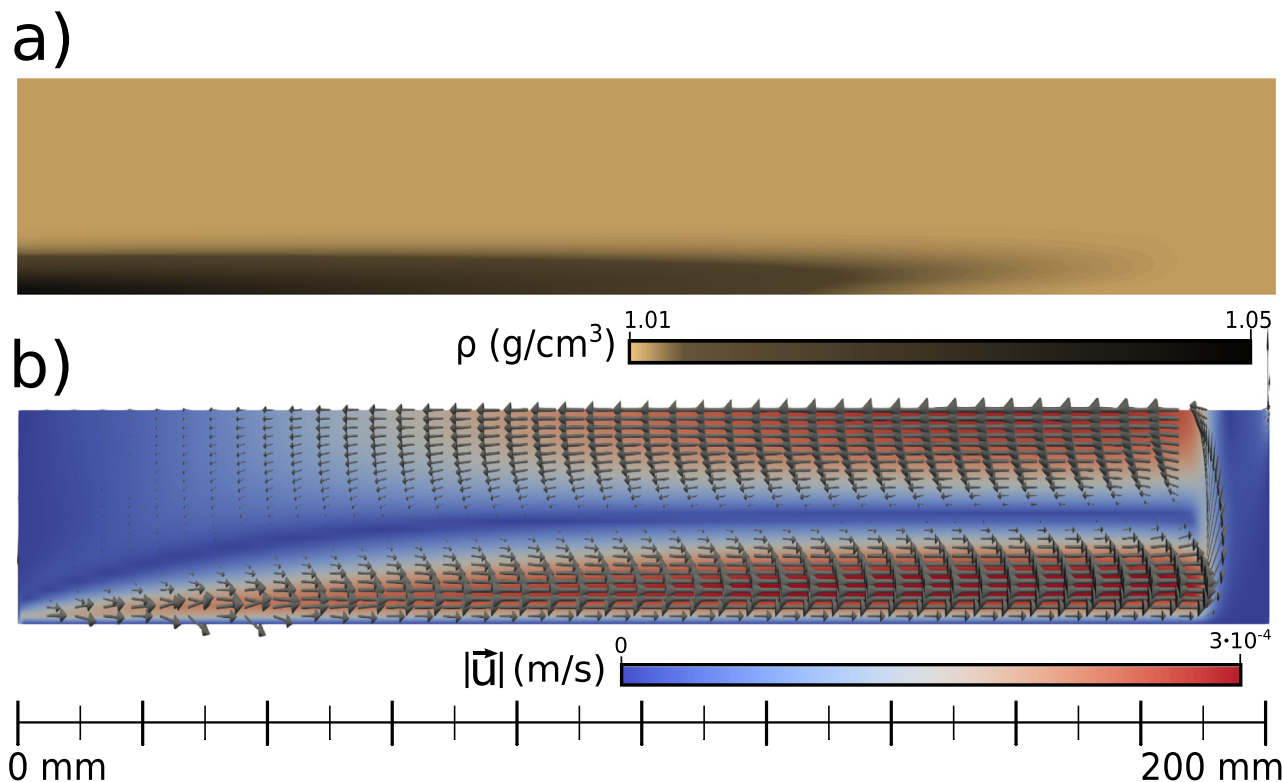


Fig. 2. The density field (a) and the flow field (b) represented also with arrow vectors at $t = 700$ s.

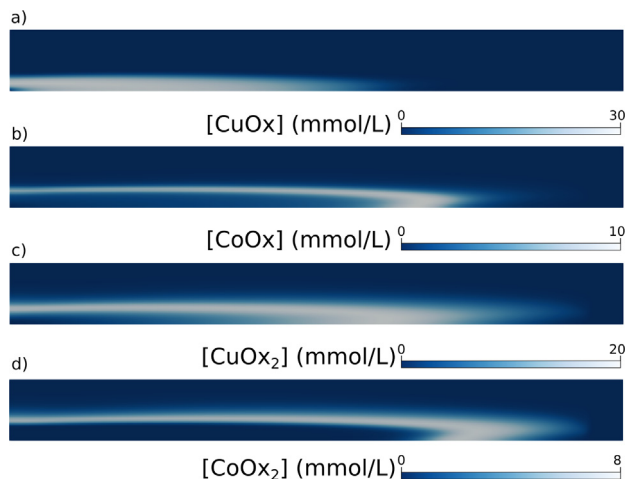


Fig. 3. Concentration distributions of a) $[\text{CuC}_2\text{O}_4]$, b) $[\text{CoC}_2\text{O}_4]$, c) $[\text{Cu}(\text{C}_2\text{O}_4)_2]^{2-}$ and d) $[\text{Co}(\text{C}_2\text{O}_4)_2]^{2-}$ complexes at $t = 700$ s.

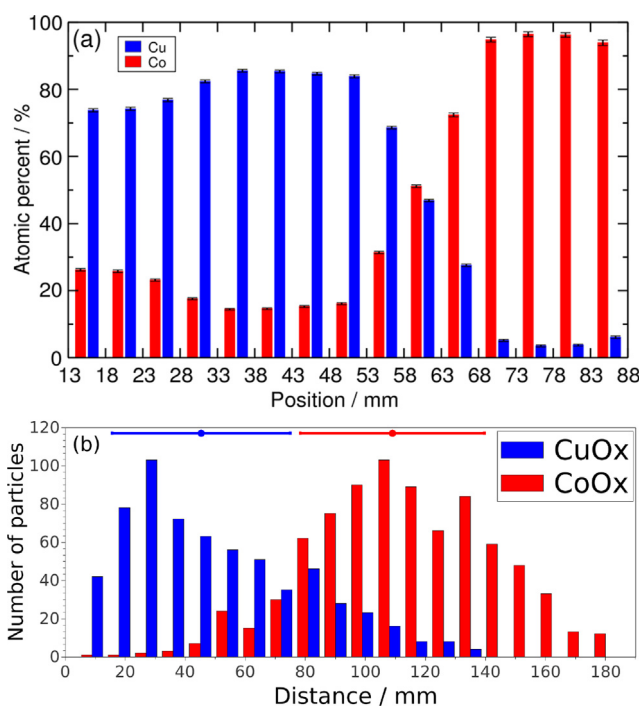


Fig. 4. (a) Reference experimental observation, reprinted (adopted) with permission from Ref. (Tth-Szeles et al., 2017). Copyright 2017 American Chemical Society. (b) Spatial distribution of the sedimented particles at $t = 700$ s. The mean position and its standard deviation for the sedimented particles are presented with a dot and a line, respectively.

where x_i is the position of the i^{th} MC particle along the x -axis, and N is the total number of particles. Solely X_{MC} is not sufficient to determine the extent of separation because the amount of individual precipitates are not given. We have excluded the cases where one of the species barely forms by examining the spatial distributions of the sedimented particles, and only concentrate on scenarios where the precipitates are in comparable amount. The calculated X_{MC} values are graphically summarized in Fig. 5 a).

An additional useful parameter to measure the goodness of spatial separation is, similarly to the enantiomeric excess, the precipitation excess (see Table 1), defined as

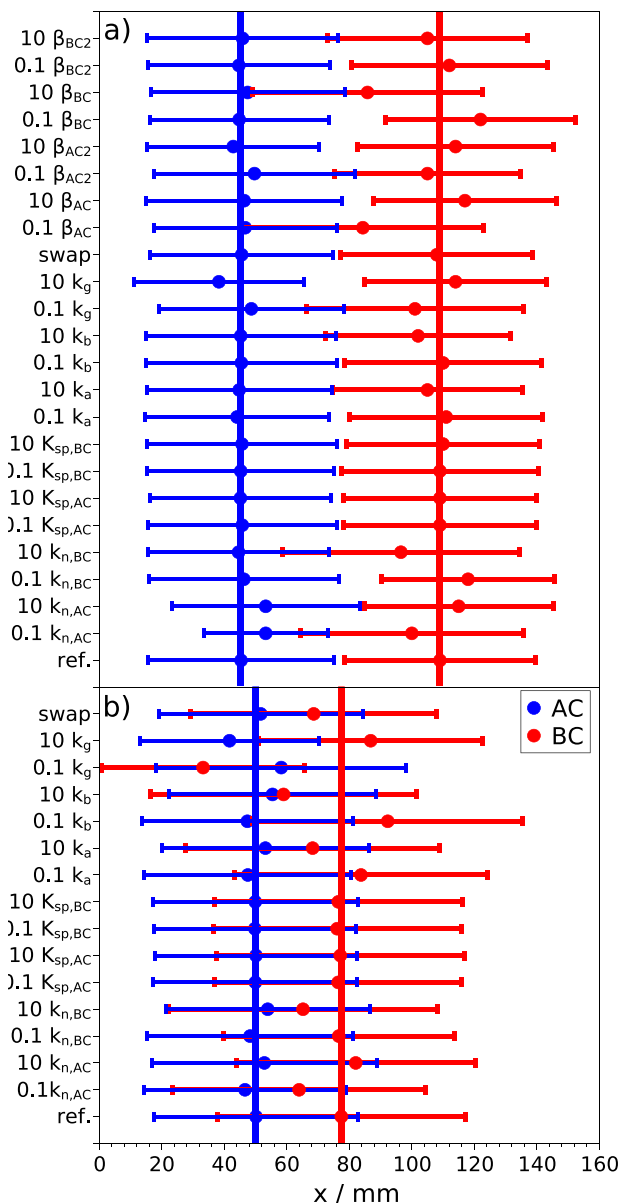


Fig. 5. The values of X_{MC} (dots) and their standard deviation (lines) with respect to the changed parameters: a) in the presence of MC (M: A, B) complex formation, b) direct precipitation in the absence of complex formation at $t = 700$ s. The straight vertical lines represent the mean of X_{MC} when the reference parameters are used.

$$pe\% = \frac{1}{K} \sum_{i=1}^K \frac{|N_{AC,i} - N_{BC,i}|}{N_{AC,i} + N_{BC,i}} 100\%, \quad (16)$$

where the space is divided into K number of equal sized (9 mm) zones along the x -axis, and $N_{AC,i}, N_{BC,i}$ are the number of AC and BC particles in the i^{th} zone, respectively. The advantage of $pe\%$ is that calculations with different set of parameters can be compared with one number instead of plotting the spatial distribution; however, it also can reach 100% when only one of the precipitates is produced in quantitative amount.

An order of magnitude shift in the value of nucleation rate coefficients will affect the amount of precipitate significantly, which can lead to cases where only one of them forms in a considerable amount with minor contamination from the other. This scenario can also be envisioned as a form of separation, however, here we focus on cases where comparable amounts of the two precipitates

Table 1

Precipitate excess (pe%) values for various parameter sets in the presence (left) and in the absence (right) of MC (M: A, B) complex formation at $t = 700$ s.

Parameter	pe% $M + C \rightleftharpoons [MC] \rightarrow MC$	pe% $M + C \rightarrow MC$
reference case	75	41
0.1 $K_{sp,AC}$	75	37
10 $K_{sp,AC}$	76	38
0.1 $K_{sp,BC}$	75	37
10 $K_{sp,BC}$	74	40
0.1 k_a	76	45
10 k_a	77	47
0.1 k_b	73	54
10 k_b	77	57
0.1 k_g	71	40
10 k_g	78	62
swap	75	39
0.1 β_{AC}	73	n/a
10 β_{AC}	78	n/a
0.1 β_{BC}	80	n/a
10 β_{BC}	69	n/a
0.1 β_{AC_2}	71	n/a
10 β_{AC_2}	78	n/a
0.1 β_{BC_2}	77	n/a
10 β_{BC_2}	71	n/a

are produced in the system. The spatial separation of them is very sensitive to the increase in the growth rate coefficient of the spherical precipitate (k_g), resulting in the faster growth of particles and causing their sedimentation closer to the inlet. For the anisometric particles, variation of either k_a or k_b will not only alter the growth of the particles but also their shapes. Calculations have also been performed for a case with k_a and k_b values swapped, however, at this flow rate and reactor geometry there is no significant effect on the spatial distribution.

Significant deviation from the reference case is not observed upon the modification of either solubility product with an order of magnitude because the very small solubility is preceded by fast complex formation. At the chosen initial concentrations, complex formation is instantaneous and the solution becomes supersaturated rapidly for both oxalate salts. Therefore, the concentration of the 1:1 complex determines the extent of supersaturation. For effective spatial separation of the final precipitates, the coupling with transport processes has to lead to the separation of these soluble complexes in advance. To test this notion, we have changed the stability constants for [AC], [AC₂], [BC] and [BC₂] complexes with one order of magnitude compared to the reference case. According to Fig. 5 a) and Table 1, the separation improves by increasing β_{AC} or β_{AC_2} or by decreasing β_{BC} or β_{BC_2} . Changing these parameters in the opposite direction worsens the spatial separation of the precipitates. In the reference case, [AC] and [BC] are analogous to [CuC₂O₄] and [CoC₂O₄], respectively, and based on the literature values $\beta_{CuOx} > \beta_{CoOx}$, therefore, $\beta_{AC} > \beta_{BC}$. Because of that, [CuC₂O₄] and [Cu(C₂O₄)₂] complexes form faster and closer to the bottom of the reactor (Fig. 3), so Co(II) ions diffuse vertically to form [CoC₂O₄] and [Co(C₂O₄)₂] complexes in the upper region of the reactor. The solid CoOx particles formed from the oxalato cobalt (II) complex remain longer in the flow and sediment further from the inlet. By increasing the difference between β_{AC} and β_{BC} (increasing β_{AC} or decreasing β_{BC}), better separation can be achieved. If the complex formation constants are close to each other, the complexes will form at the same place, and they sediment together. Moreover, a shift in β_{BC_2} value has weaker effect on the spatial separation than that in β_{BC} , which is not observable for β_{AC} and β_{AC_2} . The reason is, that according to the reference case β_{AC} is three times smaller than β_{AC_2} , however, the difference between β_{BC} and β_{BC_2} is eightfold.

In order to show that the presence of soluble complexes plays a vital role in the spatial separation of precipitates, we have considered a general system with no complex formation; a scenario typically valid for alkaline earth metal precipitates. By comparing the characteristics of the two reaction types in Fig. 5, and in cases with comparable amount of precipitates in Table 1, we see that the spatial separation is substantially worse in the absence of complexes. If both AC and BC precipitates have similar properties, the spatial distributions can even overlap completely in the absence of complexation as shown in the supplementary material.

We have also investigated the effect of flow rate with identical reactor geometry at equal spreading of the gravity current with respect to the reference case of Fig. 4. Fig. 6 illustrates that the spatial separation practically diminishes on either increasing or decreasing the flow rate with one order of magnitude compared to Fig. 4. These simulations correspond to experiments performed at 2, 20, and 200 mL/h injection rate. This indicates the existence of an optimal flow rate for a reactor size similarly to past experimental observations (Tóth-Szeles, 2018), so that time scales of transport processes can match those of the chemical reaction. Cobaltous oxalate becomes dominant at low, copper oxalate at higher flow rate when considering the number of particles (see Table 2).

Even though there is complex formation, at lower flow rate both precipitates sediment close to the inlet. Not only the number of sedimented particles is smaller at higher flow rates because of the greater fluid velocity, but also less precipitate forms in the reactor as shown in Fig. 7, where the amount of precipitate formed in the reactor (n_{MOx}) is shown as a function of injected volume (V). Initially there is always more cobaltous oxalate than copper oxalate, however, later the overall amount of copper oxalate exceeds that of cobaltous oxalate. CuOx particles nucleate closer to the bottom of the reactor, and hence, sediment sooner in contrast to the CoOx particles that are flushed away from the inlet to a greater extent. Once sedimented, CuOx particles will grow fiercely because of the positive feedback in particle growth. There is a linear relationship between the logarithm of the amount of particles ($\ln(n/mol)$) and the logarithm of the injected volume ($\ln(V/mL)$)

$$\ln(n/mol) = a \ln(V/mL) + b. \tag{17}$$

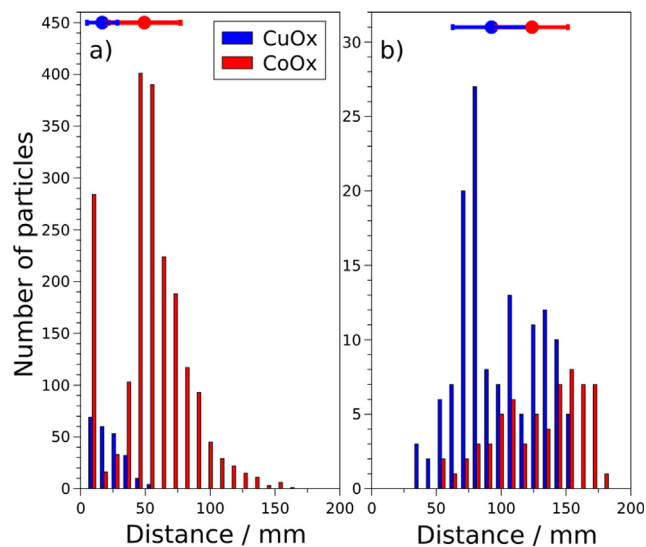


Fig. 6. The effect of different flow rates on the distribution of sedimented particles a) $u_{in} = 0.01$ mm/s at $t = 1200$ s b) $u_{in} = 1$ mm/s at $t = 200$ s, in the upper region of the graph the mean and the standard deviation in the position of sedimented particles are represented with a dot and a line, respectively. The reference case with $u_{in} = 0.1$ mm/s is shown in Fig. 4.

Table 2
The ratio of the number of sedimented particles at various injection rates.

u_{in} (mm/s)	$N_{CuOx} : N_{CoOx}$
1	68:32
0.1	44:56
0.01	10:90

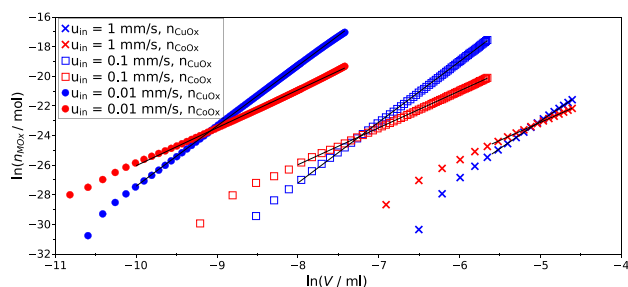


Fig. 7. Precipitate production at different injection rates.

Rearranging Eq. (17) and knowing that $V = qt$, we find that

$$n = e^b V^a = e^b q^a t^a = \beta t^a, \tag{18}$$

and by taking its temporal derivative we obtain

$$\frac{dn}{dt} = \frac{an}{t}. \tag{19}$$

Eq. (19) explicitly represents the positive feedback during particle growth because the product formation is proportional to the amount of product ($a > 0$), thus particle growth is dominant compared to nucleation, i.e., the second terms are greater than the first terms in the rate laws of Eqs. (10) and (11). The t^{-1} scaling results from the consumption of the stoichiometrically limiting oxalate ion. When comparing to single precipitate scenarios, we can see that the precipitation of CuOx is basically unaffected by the presence of cobalt(II) ions in the mixed system, whereas copper(II) ions hinder the formation of CoOx (see supplementary material). This can be rationalized by the fact that cobalt(II) oxalate complexes form in the layer above copper(II) oxalate. In the absence of copper(II) ions, cobalt(II) oxalate complexes can form closer to the bot-

tom, leading to greater gradients allowing the formation of more precipitate.

To gain a deeper understanding about the processes, we have plotted the size distributions of the total and the sedimented particles in Fig. 8, which shows that larger fraction of the produced CuOx particles remains in the reactor, compared to CoOx particles. Copper oxalate is less affected by the flow, as it nucleates closer to the bottom of the reactor and, hence, it sediments easier. Cobaltous oxalate particles nucleate in the upper region of the reactor, therefore at higher flow rate they are not able to sediment and grow; the tiny particles just drift out of the reactor. At lower flow rate, CoOx particles also sediment and grow up to 10 μm in size within the investigated time scale, while the spherical CuOx particles can reach a radius of 29 μm . The formed CoOx never exceeds the amount of CuOx produced, which is in agreement with Fig. 7.

4. Conclusions

We have constructed a reaction–diffusion–convection model for a solid–liquid system, with which we can calculate not only the concentration distribution of chemical species in the liquid phase but also the position of growing solid particles during the initial stages of a precipitation reaction. By taking equilibrium constants and solubility products from the literature without adjustment and using kinetic constants tuned for the individual precipitation processes, we have successfully modeled the mixed copper oxalate–cobalt oxalate-system, previously studied experimentally (Tth-Szeles et al., 2017; Tth-Szeles, 2018). The modeling calculations reconstruct the observations that even with comparable amount of copper(II) oxalate and cobalt(II) oxalate precipitate formed, spatial separation is achieved in a flow-driven reactor.

For a general understanding, a thorough modeling study has been carried out, by varying the flow rates, the particle shapes, and the thermodynamic and kinetic parameters to identify the factors responsible for precipitate separation in the base case. We have introduced new quantities to characterize the extent of spatial separation: mean position of the MC (M: A, B) sedimented particles (X_{MC}) and precipitation excess ($pe\%$). We have shown that the spatial distribution is sensitive to the growth rate coefficients (an experimentally inaccessible parameter), but the major factor is found to be the complex formation prior to nucleation. Without loss of generality, we have considered a domain with rectangular geometry, yet the main finding can be related to our previous experiment in a radial reactor. In that arrangement, the point source has been technically the simplest injection geometry to be implemented, but it has led to a gravity current with radially decaying spreading rate. The flow field is characterized with significantly larger fluid velocity around the inlet, unfavorable to sedimentation. Once the velocity had dropped to the optimal value, we could observe separation, similarly to the rectangular scenario.

Considering a general chemical system with two cations and a common anion, poor spatial segregation is observed independently of the kinetic and thermodynamic parameters with comparable precipitate formation in the absence of complexation. In the flow reactor the injection rate can be used to fine tune spatial separation by adjusting the time scale of transport processes to that of the precipitation reaction. Furthermore, it also alters the amount of precipitate formed in good agreement to the previous experimental study. Our reaction–diffusion–convection model is applicable not only to the industrially valuable oxalate formation in a flow-reactor but also in general to any precipitate reaction with or without complexation. An upscaling may prove the presented technique, a soluble complex prior to nucleation in a flow field, to be also feasible for industrial precipitate separation where comparable amount of precipitate forms in parallel paths.

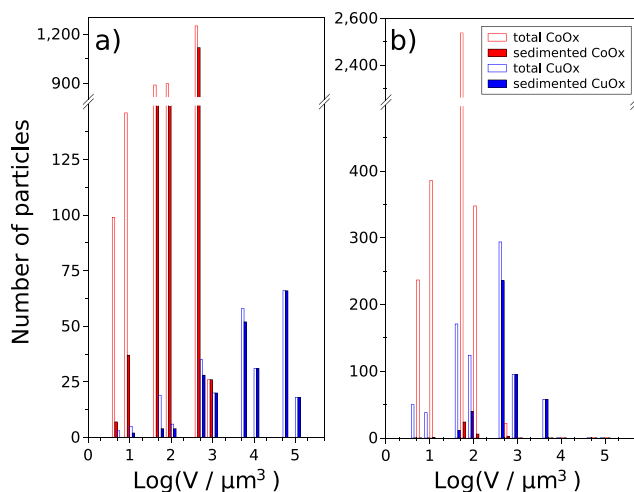


Fig. 8. Size distribution of the sedimented and the floating particles at $u_{in} = 0.01$ mm/s and $t = 1200$ s (a) and at $u_{in} = 1$ mm/s and $t = 200$ s (b) at front position 198 mm from the inlet.

CRediT authorship contribution statement

Paszkál Papp: Methodology, Software, Investigation, Writing – original draft. **Ágota Tóth:** Conceptualization, Validation, Funding acquisition, Writing – review and editing. **Dezső Horváth:** Conceptualization, Methodology, Validation, Supervision, Writing – review and editing.

Declaration of Competing Interest

The authors declare that they have no known competing financial interests or personal relationships that could have appeared to influence the work reported in this paper.

Acknowledgements

The authors gratefully acknowledge the financial support of the National Research, Development and Innovation Office (K138844). PP was supported by the ÚNKP-21-3 New National Excellence Program of the Ministry of Innovation and Technology from the source of the National Research, Development and Innovation Fund. We thank the University of Szeged Open Access Fund (5822) for support.

Appendix A. Supplementary material

Supplementary data associated with this article can be found, in the online version, at <https://doi.org/10.1016/j.ces.2022.117955>.

References

- Acarbaş, O., Suvacı, E., Doğan, A., 2007. *Ceram. Int.* 33, 537–542.
- López-Macipe, A., Gómez-Morales, J., Rodríguez-Clemente, R., 1998. *Adv. Mater.* 10, 49–53.
- Dong, X., Li, F., Zhao, N., Xiao, F., Wang, J., Tan, Y., 2016. *Appl. Catal. B* 191, 8–17.
- Jinwei, L., Yingying, Z., Fengli, M., Xingyi, L., Qi, Z., 2008. *Chinese J. Catal.* 29, 346–350.
- Coe, F.L., Evan, A., Worcester, E., 2005. *J. Clin. Investig.* 115, 2598–2608.
- Franceschi, V.R., Nakata, P.A., 2005. *Annu. Rev. Plant Biol.* 56, 41–71.
- Baker, A., Tóth, Á., Horváth, D., Walkush, J., Ali, A.S., Morgan, W., Kukovec, Á., Pantaleone, J.J., Maselko, J., 2009. *J. Phys. Chem. A* 113, 8243–8248.
- Nakouzi, E., Steinbock, O., 2016. *Sci. Adv.* 2, e1601144.
- Nabika, H., Itatani, M., Lagzi, I., 2020. *Langmuir* 36, 481–497.
- Pótári, G., Tóth, Á., Horváth, D., 2019. *Chaos* 29, 073117.
- Brau, F., Schusztter, G., De Wit, A., 2017. *Phys. Rev. Lett.* 118, 134101.
- Rakotozandriny, K., Bourg, S., Papp, P., Tóth, Á., Horváth, D., Lucas, I.T., Babonneau, F., Bonhomme, C., Abou-Hassan, A., 2020. *Cryst. Growth Des.* 20, 7683–7693.
- Bohner, B., Schusztter, G., Horváth, D., Tóth, Á., 2015. *Chem. Phys. Lett.* 631–632, 114–117.
- Olgun, A., Atar, N., 2011. *Chem. Eng. J.* 167, 140–147.
- Cisternas, L.A., Vásquez, C.M., Swaney, R.E., 2006. *AIChE J.* 52, 1754–1769.
- Ito, Y., Qi, L., 2010. *J. Chromatogr. B* 878, 154–164.
- Zhang, Y., Tang, J., Liu, S., Hu, F., Liu, M., Jin, W., Hu, J., 2020. *Sep. Purif. Technol.* 240, 116625.
- Duan, H., Wang, Z., Yuan, X., Wang, S., Guo, H., Yang, X., 2017. *Sep. Purif. Technol.* 173, 323–329.
- Diabate, P.D., Boudesocque, S., Mohamadou, A., Dupont, L., 2020. *Sep. Purif. Technol.* 244, 116782.
- Li, N., Li, Q., Guo, X., Yuan, M., Pang, H., 2019. *Chem. Eng. J.* 372, 551–571.
- Bowen, P., Pujol, O., Jongen, N., Lemaitre, J., Fink, A., Stadlerman, P., Hofmann, H., 2010. *Nanoscale* 2, 2470–2477.
- Yamada, E., Murakami, H., Nishihama, S., Yoshizuka, K., 2018. *Sep. Purif. Technol.* 192, 62–68.
- Prieto, G., Beijer, S., Smith, M.L., He, M., Au, Y., Wang, Z., Bruce, D.A., de Jong, K.P., Spivey, J.J., de Jongh, P.E., 2014. *Angew. Chem. Int. Ed.* 53, 6397–6401.
- Xiang, Y., Barbosa, R., Kruse, N., 2014. *ACS Catal.* 4, 2792–2800.
- Chen, C., Liu, L., Li, Y., Li, W., Zhou, L., Lan, Y., Li, Y., 2020. *Chem. Eng. J.* 384, 123257.
- Adamo, P., Violante, P., 2000. *Appl. Clay Sci.* 16, 229–256.
- Sarret, G., Manceau, A., Cuny, D., Van Haluwyn, C., Déruelle, S., Hazemann, J.-L., Soldo, Y., Eybert-Bérard, L., Menthonnex, J.-J., 1998. *Environ. Sci. Technol.* 32, 3325–3330.
- Fomina, M., Hillier, S., Charnock, J.M., Melville, K., Alexander, I.J., Gadd, G.M., 2005. *Appl. Environ. Microbiol.* 71, 371–381.
- Kaewdoug, B., Sutjaritvorakul, T., Gadd, G.M., Whalley, A.J., Sihanonth, P., 2016. *Geomicrobiol. J.* 33, 283–288.
- Gadd, G.M., 2007. *Mycol. Res.* 111, 3–49.
- Stergiou, Y., Eckert, K., Schwarzenberger, K., 2022. *Chem. Eng. J.* 428, 131146.
- Tóth-Szeles, E., Bohner, B., Tóth, Á., Horváth, D., 2017. *Cryst. Growth Des.* 17, 5000–5005.
- E. Tóth-Szeles, Ph.D. dissertation, University of Szeged, 2018, <https://doktori.bibl.u-szeged.hu/id/eprint/9880>
- Haider, A., Levenspiel, O., 1989. *Powder Technol.* 58, 63–70.
- Das, N.P., Zahorán, R., Janovák, L., Imre-Deák, A., Tóth, Á., Horváth, D., Schusztter, G., 2020. *Cryst. Growth Des.* 20, 7392–7398.
- Mullin, J.W., 2001. *Crystallization*. Butterworth-Heinemann, Oxford.
- Weller, H.G., Tabor, G., Jasak, H., Fureby, C., 1998. *Comput. Phys.* 12, 620–631.
- Issa, R., 1986. *J. Comput. Phys.* 62, 40–65.
- Kotrlý, S., Sucha, L., 1985. *Handbook of Chemical Equilibria in Analytical Chemistry*. Ellis Horwood Ltd., Chichester.